Layered organization of anisometric cellulose nanocrystals and beidellite clay particles accumulated near the membrane surface during cross-flow ultrafiltration: In situ SAXS and ex situ SEM/WAXD characterization

Enrico Semeraro, Nicolas Hengl, Mohamed Karrouch, Laurent Michot, Erwan Paineau, Bruno Jean, Jean-Luc Putaux, Christine Lancelon-Pin, Lewis Sharpnack, Frédéric Pignon

Layered organization of anisometric cellulose nanocrystals and beidellite clay particles accumulated near the membrane surface during cross-flow ultrafiltration: *in situ* SAXS and *ex situ* SEM / WAXD characterization

Enrico F. Semeraro[1], Nicolas Hengl[1], Mohamed Karrouch[1], Laurent J. Michot[2], Erwan Paineau[3], Bruno Jean[4], Jean-Luc Putaux[4], Christine Lancelon-Pin[4], Lewis Sharpnack[5] and Frédéric Pignon[1]*

[1]Univ. Grenoble Alpes, CNRS, Grenoble INP (Institute of Engineering Univ. Grenoble Alpes), LRP, F-38000 Grenoble, France

[2]Sorbonne Univ., UPMC, UMR 8234, Lab. Phenix, CNRS, 4 Pl. Jussieu, F-75252 Paris 5, France

[3]Univ. Paris Saclay, Univ. Paris Sud, CNRS, Lab. Phys. Solides, F-91405 Orsay, France

[4]Univ. Grenoble Alpes, CNRS, CERMAV, F-38000 Grenoble, France

[5]ESRF, The European Synchrotron, CS 40220, F-38043 Grenoble Cedex 9, France

Corresponding author: frederic.pignon@univ-grenoble-alpes.fr

Abstract

The structural organization of the concentration polarization layer (CPL) during the cross-flow membrane separation process of anisometric aqueous suspensions of colloidal cellulose nanocrystals and beidellite clay particles has been characterized by *in situ* time-resolved small-angle X-ray scattering (SAXS). Dedicated cross-flow filtration cells were implemented on the ID02 TRUSAXS beamline at the European Synchrotron Radiation Facility (Grenoble, France). From the analysis of the scattered intensities and structure factors of particles in the CPL, both the concentration profiles $\phi(\Delta z,\Delta t)$ and anisotropic structural organization have been characterized as a function of filtration time (Δt) and distance from the membrane surface (Δz). Remarkably, a coupling between concentration and anisotropy was revealed and modeled using either a simple or stretched exponential trend for rod- or disk-like systems, respectively. Using a simple filtration model, the time evolution of the deposit thickness, membrane resistance and specific resistance of the deposit, deduced from an analysis of the normalized concentration profiles, allowed directly predicting the rapid decay of permeate flux associated to the exponential growth of concentration and anisotropic organization inside the CPL. *Ex situ* scanning electron microscopy (SEM) observations and wide-angle X-ray diffraction (WAXD) analyses performed on dried deposits parallel and perpendicular to the membrane surface revealed well-defined layered structures from nanometer to micrometer length scales.

Keywords: cross-flow ultrafiltration, concentration polarization layer, SAXS, anisotropic colloids, cellulose nanocrystals, clay particles, permeation flux.

Introduction

Membrane separation processes are widely used in industrial applications (bio-industries, agro-industries, or sludge treatment) for concentrating and purifying nanoparticle dispersions.[1] Under the action of the transmembrane pressure and cross-flow velocity, the particles accumulate near the membrane surface in the so-called concentration polarization layer (CPL) and their concentration can rise above the sol-gel transition, leading to a catastrophic loss in permeability. Consequently, an accurate understanding of the structural organization of colloids in the CPL in parallel with the filtration properties is of considerable interest to improve the efficiency of the filtration. Depending on the transmembrane pressure and cross-flow conditions, a transition from stable to unstable filtration performance has been identified and a limit has been proposed in the literature.[2,3] The authors have identified a critical flux, which determines the transition from a reversible CPL to an irreversible deposit formation. Colloidal interactions and osmotic pressure have been identified as pertinent parameters and have been introduced in models to describe this transition.[4-12] It has only been recently possible to access the evolution of the concentration within the CPL as a function of time, distance from the membrane surface and filtration conditions by combining dedicated cross-flow ultrafiltration cells and *in situ* small-angle X-ray scattering (SAXS) measurements.[13-16] Thanks to this unique method, it is now possible to finely investigate the colloidal concentration profile as well as the anisotropic organization at the micrometer scale and relate these quantities to the permeate flux reduction during cross-flow ultrafiltration.

In this work, we studied the mechanisms involved in the sol-gel transition that takes place during the cross-flow ultrafiltration of anisotropic colloidal suspensions. From a filtration point a view, the questions raised are the following: *i)* what are the sol/gel phase-transition mechanisms involved during the ultrafiltration processes when anisotropic colloids are simultaneously submitted to shear flow and pressure near the membrane surface? *ii)* Which link

66 can be established between the permeation flux and the space- and time-dependent evolutions
67 of the deposit formation (accounting for thickness, concentration, particle orientation and
68 specific resistance)? Finally, we evaluated the extent to which a prediction of the permeate flux
69 could be achieved by a direct analysis of the dynamic evolution in space and time of the colloids
70 accumulated near the membrane surface, using *in situ* SAXS data.

71 To answer these questions, two types of anisometric particles (rod- and disk-like) have been
72 considered. The rod-like system consisted of cellulose nanocrystals (CNCs),[15] prepared by
73 strong acid hydrolysis of native wood cellulose microfibrils. Their average dimensions are
74 typically 10 nm in width and 100-200 nm in length (Fig. 1A) and thanks to the presence of
75 charged sulfate groups at their surface, they can form chiral nematic (cholesteric) organizations
76 in aqueous suspension.[17,18] CNCs are particularly attractive building blocks for the design of
77 innovative biobased materials and with numerous potential applications such as
78 environmentally-friendly nanocomposites, paper coating or biomedical products.[19-21] CNCs
79 display outstanding mechanical properties such as a modulus as high as 120-150 GPa and a
80 strength up to 6 GPa and are now commercially available in large quantities. The disk-like
81 system is composed of natural beidellite clay particles (Fig. 1B) which are subhedral lamellae
82 (typically 1 nm-thick and 300-500 nm-wide). Like other swelling clays like montmorillonite,
83 beidellite is a ubiquitous mineral on the Earth's surface and subsurface and is largely used for
84 industrial (drilling fluids, anti-settling agents, ointments, cosmetics, and health)
85 applications.[17,22,23]

86 The space and time dependence of particle concentration and structural organization within
87 the accumulated layers of CNCs or beidellite particles deposited near the membrane surface,
88 have been characterized by *in situ* SAXS experiments during cross-flow filtration and linked to
89 the filtration properties of the dispersions. Specific analyses of concentration, anisotropy and
90 principal orientation direction of the particles, have allowed to link these different parameters

and to provide a straightforward prediction using a simple filtration model of the rapid decay of the permeate flux at the initiation of the deposit growth and its corresponding specific resistance. The comparison of these results obtained on the two studied systems, namely CNCs and beidellite clay particles, is used to bring some highlights on the potential links between filtration parameters (thickness, resistance and permeate flux) and physical features (colloidal volume fraction, orientation, shape and aspect ratio).

The organization built during cross-flow ultrafiltration was consolidated via dead-end ultrafiltration, followed by air-drying of the deposits. The structure of the solid deposits was characterized *ex situ* using wide-angle X-ray diffraction (WAXD) and scanning electron microscopy (SEM) both parallel and perpendicular to the membrane surface, which allowed evaluating the degree of orientation of the constituting particles in the textured materials.

Materials and Methods

Materials

Cellulose nanocrystals (CNCs) were purchased from UMaine Development Center (University of Maine, USA) as a suspension in water with a stock concentration of c = 12.2 wt%. Suspensions at c_0 = 0.7 wt% were prepared by diluting the stock suspension with deionized water, followed by 2 h of vigorous stirring. CNC aggregates were fragmented by using a sonication probe (Branson Digital sonifier) applying a minimum of 2 kJ per gram of CNCs.[24] Considering the CNC density (1.6 g cm^{-3}), the final suspension had a nominal volume fraction of $\phi_0 \simeq 0.0044$.

Natural beidellite (SBId-1) clay powder was purchased from the Idaho Source Clays Minerals Repository of the Clay Mineral Society (Purdue University). Beidellite suspensions were purified of extra minerals and centrifugation was used for size fractionation (the detailed sample preparation has been described by Paineau et al.[17,23]). The dilute suspension had an ionic

strength of 10^{-4} M and a concentration of about c_0 = 0.8 wt%, corresponding to a volume fraction of about ϕ_0 = 0.0031 (beidellite density 2.6 g cm^{-3}).[23,25]

Transmission Electron Microscopy (TEM)

Droplets of dilute CNC or beidellite aqueous suspensions were deposited onto glow-discharged carbon-coated copper grids and allowed to dry. The specimens were observed with a JEOL JEM-2100-Plus microscope operating at an accelerating voltage of 120 kV. Images were recorded with a Gatan Rio 16 camera equipped with the GMS acquisition software. In Figure 1A, the TEM image of the CNC is presented, revealing elongated objects constituted of rod-like crystallites of a few units.[24] In Figure 1B, the TEM image of beidellite clay particles reveals a typical platelet shape exhibiting irregular facetted contours. [23,25]

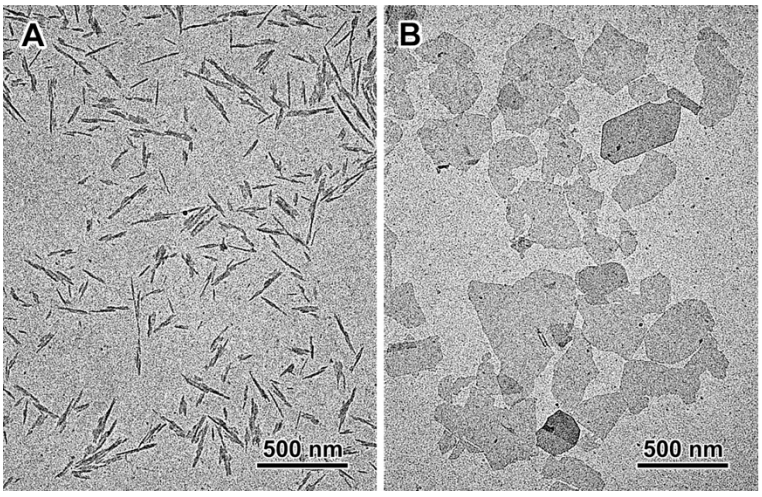

Figure 1. TEM images of the CNCs (A) and beidellite clay particles (B) used in this study.

Small-Angle X-ray Scattering (SAXS)

SAXS measurements were performed at the TRUSAXS ID02 beamline (ESRF, Grenoble).[26] Measurements were performed at room temperature with a sample-detector (RayoniX MX170) distance of 10 m and an X-ray wavelength λ = 0.095 nm, covering a range of scattering vector amplitude, q, of (0.01−0.5) nm^{-1}. Thanks to the pinhole collimation setup available at ID02, all the measurements were acquired by using a vertical beam cross-section at the sample position

of about 30 μm, hence corresponding to the maximum resolution of the membrane distance Δz. The two-dimensional scattering patterns were corrected and normalized to absolute scale.

A temperature-controlled flow-through capillary cell (diameter = 1.85 mm) was used to measure the absolute scattered intensity of dispersions at rest at T = 22 °C. Sample and background scattering were measured at the same position of the capillary, thus allowing a very reliable subtraction. The normalized background scattering of the flow-through capillary cell and cross-flow ultrafiltration cell filled with distilled water were systematically subtracted prior to data analysis. Then, scattering intensities as a function of q were obtained by azimuthally averaging isotropic scattering patterns. In the case of anisotropic signals (Fig. 3A), scattering intensities along a defined scattering angle ψ (either $\psi = 0$ or $\pi/2$) were obtained by azimuthally averaging such patterns around the angle of interest over a narrow sector of ±0.044 rad (±2.5°).

Preparation of textured solid deposits

The protocol used to prepare air dry deposit is the following. In a first step, a cross-flow ultrafiltration identical of the one performed under *in-situ* SAXS at cross-flow flux Q = 0.06 L min^{-1} and transmembrane pressure $\Delta P = 1.1 \times 10^5$ Pa was achieved during 2 h. The deposits were further consolidated by continuing the filtration in dead-end ultrafiltration, i.e. the cross-flow was arrested while ΔP remained unchanged. This second step of dead-end ultrafiltration was applied for about 20 h to consolidate the structural organization induced during the first step. Then, the suspensions were gently removed from the filtration cell and tubing by using compressed air (ΔP = 0.1 bar) and the gel-like deposits were extracted from the filtration cell. Finally, as a third step, samples were dried at ambient conditions for several days for further ex situ structural analyses.

Wide-Angle X-ray Diffraction (WAXD)

Strips of solid specimens were cut with a razor blade and fixed on 0.2 mm collimators in such a way that the plane of the film was oriented parallel or perpendicular to the X-ray beam. The specimens were analyzed in a Warhus vacuum chamber using a Philips PW3830 generator operating at 30 kV and 20 mA (Ni-filtered CuKα radiation, $\lambda = 0.1542$ nm). Two-dimensional patterns were recorded on Fujifilm imaging plates read with a Fujifilm BAS 1800-II bioimaging analyzer.

Scanning Electron Microscopy (SEM)

The solid deposits were fractured at room temperature and the fragments were fixed on metallic stubs covered with carbon tape. The fracture surfaces were coated with Au/Pd in a Baltec MED 020 sputter coater and the various surfaces were observed in secondary electron mode with a FEI Quanta-FEG 250 microscope operating at an acceleration voltage of 2 kV.

Cross-Flow Ultrafiltration under SAXS

A tailored cross-flow ultrafiltration cell was employed for SAXS experiments. It consisted of a PTFE channel for the permeate and a polycarbonate upper channel for the retentate (Fig. 2). The polycarbonate block exhibited a 500 µm-thick window in the center of the upper channel to minimize X-ray absorption. The two channels were separated by a flat polysulfone ultrafiltration membrane (100 kD, Pleyade Rayflow x100, Orelis Environnement, membrane resistance $R_m \sim 5 \times 10^{12}$ m^{-1}) placed on a rigid, perforated substrate to avoid pressure-induced deformations. The length of the retentate channel was 100 mm along the tangential flow (Q) direction, with a section of 8 mm in height and 4 mm in depth (along the X-ray beam direction).

The transmembrane pressure, ΔP, was measured at the entry of the cell with a pressure gauge (FP 110 FGP Sensors & Instrument) and set to $\Delta P = 1.1 \times 10^5$ Pa. Pressure was applied to the rig via purified compressed air. The feed suspension was pumped (Mono pump LF series, Axflow) from a high pressure resistant vessel (Millipore, France) to the ultrafiltration cell.[14,15] The feed cross-flow rate was imposed at $Q = 0.06$ L min^{-1} and measured with a magnetic flow

meter (Optiflux 6300C, KROHNE, France). The permeate flux, J_p, was continuously recovered in a recipient and its mass was registered with a computer every 10 s with a scale of 0.001 g of accuracy (Precisa 400M). During SAXS measurements, the cell was mounted on a motorized sample stage, which enabled *i*) aligning the membrane plane parallel to the X-ray beam and *ii*) vertically translating the cell across the incident beam in order to follow the evolution of the colloidal structure as a function of membrane distance Δz.

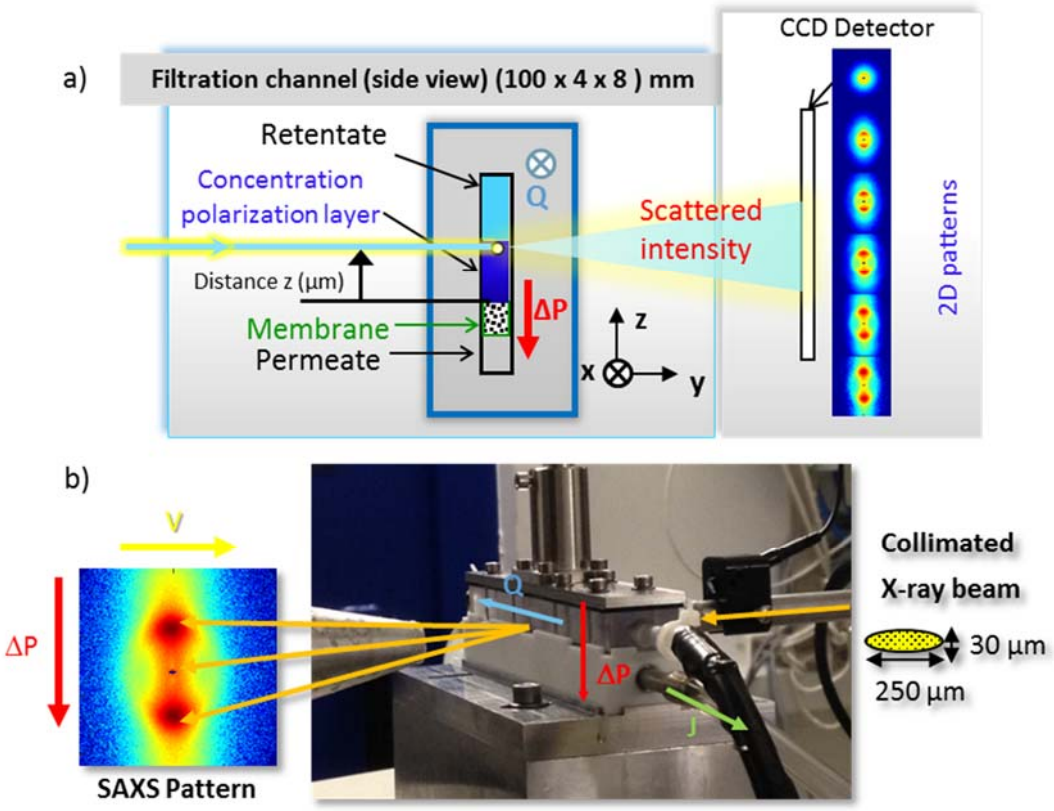

Figure 2: a) Schematic description, and b) picture and of the SAXS cross-flow ultrafiltration cell positioned on the ID02 TRUSAXS beamline at the ESRF. The arrows define the corresponding directions of the cross-flow Q, transmembrane pressure ΔP, permeate flux J, velocity v, related to the X-ray beam propagation and scattered intensity recorded on the CCD detector. The retentate flows in the upper channel (polycarbonate), which has a 500 µm-thin window in the center to minimize X-ray absorption. The solvent passes through the ultrafiltration membrane and reaches the permeate channel (PTFE). The membrane is supported by a grid with a honeycomb structure, preventing any pressure-induced deformation of the membrane and CPL.

In situ SAXS measurements were performed during the whole filtration process, in order to follow the evolution of both colloidal concentration and particle orientation. The analysis of the anisotropy (in this case related to the preferential orientation of the colloids) was performed by using the MATLAB-based Small-Angle Scattering Evaluation Tool (SASET) software.[27] Specifically, the model-free Principal Component Analysis (PCA) method was chosen, which provides values from 0 (for isotropic suspensions) to 1 (in the case of completely aligned systems). The anisotropy and direction of maximum scattering (ψ_0) were calculated via PCA in the (0.045 - 0.5) nm^{-1} q-range. The determination of the colloidal volume fraction was performed by exploiting specific properties of both CNCs and beidellite particles. These are both negatively charge-stabilized colloids, that show well-defined scattering structure-factors of interaction [$S(q)$] even at moderately low volume fraction.[18,22,23,28]

Results and Discussion

Structure Factor and Calibration of Cellulose Nanocrystal Scattering Intensity

In order to analyze the scattering intensities [$I(q)$] in the cross-flow ultrafiltration cell, a calibration curve has to be established. It relates the absolute $I(q)$ of cellulose nanocrystals to the volume fraction in the suspension via the peak position of their structure factor $S(q)$. Thanks to this calibration procedure, *in-situ* scattering intensities measured in the cross-flow ultrafiltration cell at different filtration times and distances from the membrane surface, allowed calculating the volume fractions $\phi(\Delta z,\Delta t)$ of the filtered suspension near the membrane surface. In this aim, several CNC samples at different volume fractions were first measured by SAXS in static conditions in flow-through cell, in order to obtain the calibration curve, which uniquely defines the particle concentration as a function of the peak position of $S(q)$ (Supporting Information Fig. S1).[28] Due to the strong repulsive electrostatic interactions between CNCs in

aqueous suspensions,[18] scattering intensities from CNC suspensions exhibited a visible structure factor even at the lowest concentration $\phi_0 \simeq 0.0044$ (Fig. 3B, $\Delta t = 0$). Hence, during cross-flow measurements, the effective ϕ of CNC colloids was extracted through the evaluation of the peak position of $S(q)$ at each position Δz and time step Δt (Δt was set to 0 when the transmembrane pressure ΔP was applied).

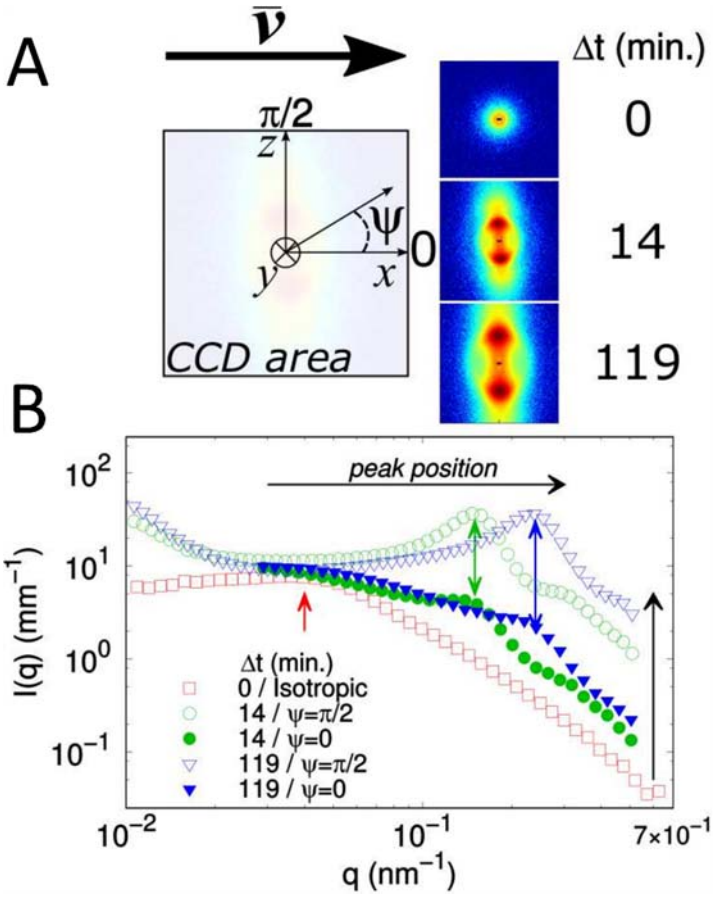

Figure 3: (A) Left: example of scattering pattern in the xz plane of the CCD detector. The scattering angle ψ is null in the direction of the velocity field of the retentate. Right: representative evolution of the scattering pattern of CNC under filtration at $\Delta z = 30$ µm and $\Delta t = 0$, 14 and 119 min. (B) Scattering intensities I as a function of q. The isotropic pattern at $\Delta t = 0$ min was azimuthally averaged, whereas data at $\Delta t = 14$ and 119 min were averaged around two directions of interest. Arrows point out the shift of the peak position as a function of time.

Selected scattering patterns are shown in Figure 3. At $\Delta t = 0$, the scattering pattern is isotropic and the azimuthally averaged *I(q)* exhibits a peak at about $q \simeq 0.04$ nm^{-1}. In contrast, during filtration, scattering patterns close to the membrane display a significant anisotropy (Fig. 3B). The maximum scattering direction is alongside $\psi \sim \pi/2$, demonstrating that CNC nanorods are preferentially oriented parallel to the membrane surface (*xy*-plane) with their main axis in the direction of the flow. Scattering curves at $\psi = 0$ and $\pi/2$ are shown in Figure 3B. The peak positions shift as a function of time, reflecting how the colloidal concentration increases during the filtration process. Interestingly, the *q*-positions of the peaks at $\psi = \pi/2$ are systematically consistent with the broader ones at $\psi = 0$. In the hard-sphere model (as an approximation of a repulsive potential), the *q*-value corresponding to the peak of *S(q)* is related to the interparticle distance via the relation $2\pi/q_{peak}$. Therefore, as the peak positions at $\psi = 0$ and $\pi/2$ are matching, the average interparticle distances along both *z*- and *x*-directions are also comparable. Thanks to this, the effective volume fraction can be reliably deduced from q_{peak}, even in the case of an anisotropic scattering pattern. This important information allowed us to retrieve actual colloidal concentrations in the ultrafiltration cell through the *q*-positions of the peaks of *I(q)* regardless the anisotropic feature of the scattering pattern.

Ultrafiltration of Cellulose Nanocrystal Suspensions

In Figure 4A, the concentration of CNCs as a function of the distance from the membrane, $\phi(\Delta z, \Delta t)$, is reported for different time steps. Distinctly, an increase of concentration is observed from the first few minutes of filtration. At each time step, the concentration profiles systematically follow a single exponential decay:

$$\phi(\Delta z, \Delta t) = \phi_0 + \phi(0, \Delta t) e^{-\frac{\Delta z}{\zeta_c(\Delta t)}} \quad (1)$$

where $\zeta_c(\Delta t)$ is the time-dependent characteristic length of the exponential decay (Supporting Information Table S1) and $\phi(0,\Delta t)$ is the time-dependent colloidal volume fraction at the

membrane position (Δz=0). Both quantities were determined by data fitting (Figure 4A). Such an exponential concentration profile is consistent with the solution of the particle mass balance equation given by:

$$D(x,t)\,\frac{\partial \phi(x,z,t)}{\partial z} + \tilde{J}_p(x,t)\phi(x,z,t) = 0 \qquad (2)$$

where $\tilde{J}_p(x,t)$ and *D(x,t)*are the permeate flux and average diffusion coefficient of the particles within the concentrated layer at the cell position *x* and time *t*.[29] Equation 2 is obtained under a few assumptions, including *i*) much smaller average particle dimensions compared to the concentrated-layer thickness; *ii*) much smaller permeate flux compared to cross-flow velocity; *iii*) negligible convection on the x-axis within the concentrated-layer; and *iv*) zero particle-transport at the membrane surface (Δz = 0). Essentially, CNC concentration profiles in Figure 4A describe well-defined concentrated layers with their flowing particles that obey a "model" particle mass-balance for hard-spheres dispersions. Moreover, this description is valid for each observed Δt. One could note that, within the framework of this model, the obtained characteristic length, ζ_c, can be used to extrapolate information about the diffusion coefficient, as $\zeta_c(t) = D(x,t)\tilde{J}_p(x,t)$. However, in the experiments reported in this work, the measured $J_p(t)$ is the total permeate flux, which is averaged over the full *x*-axis. Another interesting feature highlighted by these *in-situ* measurements is that the deposited layers undergo no compaction of the deposit all along the concentration phenomena. Indeed, the measured concentration profiles show regular accumulation of particles from the membrane surface Δz = 0 until increasing Δz positions and this for each Δt filtration time. That is to say that, at each filtration time, all the layers accumulated above the membrane surface concentrate regularly.

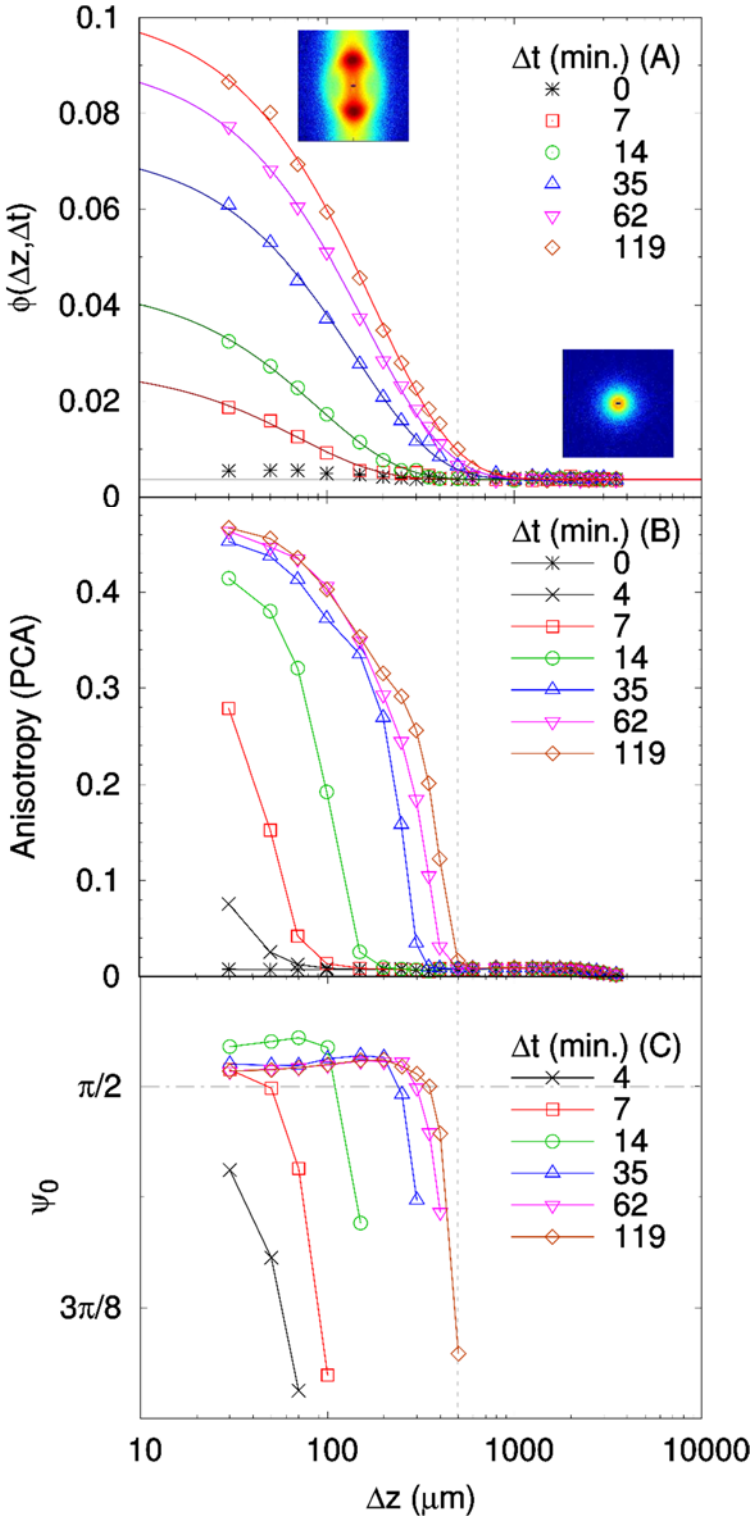

280

281 **Figure 4:** Concentration (A), anisotropy (B) and maximum scattering direction (C) profiles of the
282 growing CNC deposit as a function of Δz at different time steps. Solid lines in panel (A) refer to the
283 fitting performed with Eq. 1. The two-dimensional scattering patterns in (A) corresponds to Δz = 30 μm
284 at Δt = 0 (right) and 119 min (left). The vertical dotted line highlights the coupling between
285 concentration and anisotropy and marks the edge of the deposit. Note that ψ_0 is not defined for isotropic
286 scattering patterns.

If a compaction of the deposited layers would appear at a certain filtration time, this regular particle accumulation from the membrane surface would exhibit a change in the single exponential decay features highlighted on these concentrating phenomena. This change has not been observed, as the single exponential decay persisted all along the concentration phenomena. Consequently, no occurrence of compaction of one part of the deposited layers has been evidence in the studied filtration conditions.

Anisotropy parameters and maximum scattering direction, ψ_0, calculated via PCA are presented in Figures 4B and 4C, respectively. Although the concentration profile continuously decreases as a function of Δz, a sharp fall in both anisotropy and ψ_0 is observed. Such a behavior can provide a direct observation of the edge of the structured CPL, which systematically corresponds to a threshold in volume fraction of $\phi \sim 0.01$. Below this value, the trend of the anisotropy values seems strongly linked to the concentration profile and the formation of a concentrated, oriented layer of a few tens of micrometers is already visible after 4 min of filtration. However, ψ_0 is stabilized at about 1.6 rad after $14 - 35$ min. In the steady state, the average orientation of CNC nanorods is then slightly tilted with regard to the membrane plane. This deviation may be associated to the shape of the deposit in the *xz*-plane, which likely results from a different rate of colloidal accumulation alongside *x*.[14,29]

Concentration profiles, $\phi(\Delta z,\Delta t)$, plotted as a function of time are shown in Figure 5. Also in this case, these curves can be described by a single exponential increase:

$$\phi(\Delta z, \Delta t) = \phi_0 + \phi^{\infty}(\Delta z)\left[1 - e^{-\frac{(\Delta t - t_0)}{\tau_c(\Delta z)}}\right] \quad (3)$$

where $\phi^{\infty}(\Delta z) \equiv \phi(\Delta z, \Delta t \rightarrow \infty)$ is the limiting volume fraction that the deposit can achieve at a given Δz. The value $\tau_c(\Delta z)$ is the characteristic time of the exponential increase, whereas $t_0(\Delta z)$

depicts the moment when any variation from ϕ_0 start to be detectable. The $\phi^{\infty}(\Delta z)$, $\tau_c(\Delta z)$ and $t_0(\Delta z)$ values were obtained from the fits shown in Figure 5.

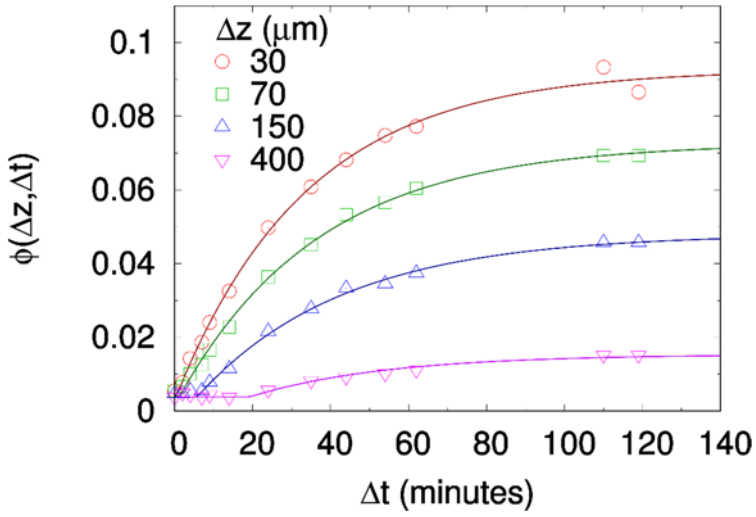

Figure 5: Concentration profiles of the growing CNC deposit as a function of Δt at different distances from the membrane. Solid lines refer to the fitting performed with Eq. 3.

Ultrafiltration of Beidellite Suspensions

Like CNC nanorods, beidellite platelets are electrostatically stabilized in aqueous suspensions. Above the liquid/gel transition ($0.005 < \phi < 0.0075$),[22] the strong repulsive interaction is responsible for the observation of the scattering structure factor $S(q)$ (Fig. 6).

Approximating the repulsive interaction as a hard-sphere potential allows determining the interparticle distance as $d = 2\pi/q_{max}$, where q_{max} is the peak position of $S(q)$. The interparticle distance was then used to determine the effective colloidal volume fraction, ϕ, from the swelling law $\phi(d)$ as described by Paineau and coworkers.[23,25]

Unfortunately, at low ϕ, below the gel transition, no interaction peak was observed. In these cases, effective ϕ values were calculated by fitting scattering curves along ψ_0 and $\psi_0 - \pi/2$. The analysis was performed by using a monodisperse scattering form factor for disks, given by:

$$F(q,\psi,\theta,\varphi) = \phi V \Delta\rho^2 \left\{ 2 \frac{\sin[qa\cos(\gamma)/2]}{qa\cos(\gamma)/2} \frac{J_1[qR\sin(\gamma)]}{qR\sin(\gamma)} \right\}^2 \quad (4)$$

where:

$$\cos(\gamma) = \cos(\psi)\cos(\theta) + \sin(\psi)\sin(\theta)\cos(\varphi) \quad (5)$$

and using the Maier-Saupe orientation distribution function (ODF)[30] to perform the orientation averaging:

$$I(q,\psi) = (2\pi N)^{-1} \int_0^{\pi/2} \mathrm{d}\theta \int_0^{\pi} \mathrm{d}\varphi \, F(q,\psi,\theta,\varphi) e^{m\cos(\theta)^2} \sin(\theta) \quad (6)$$

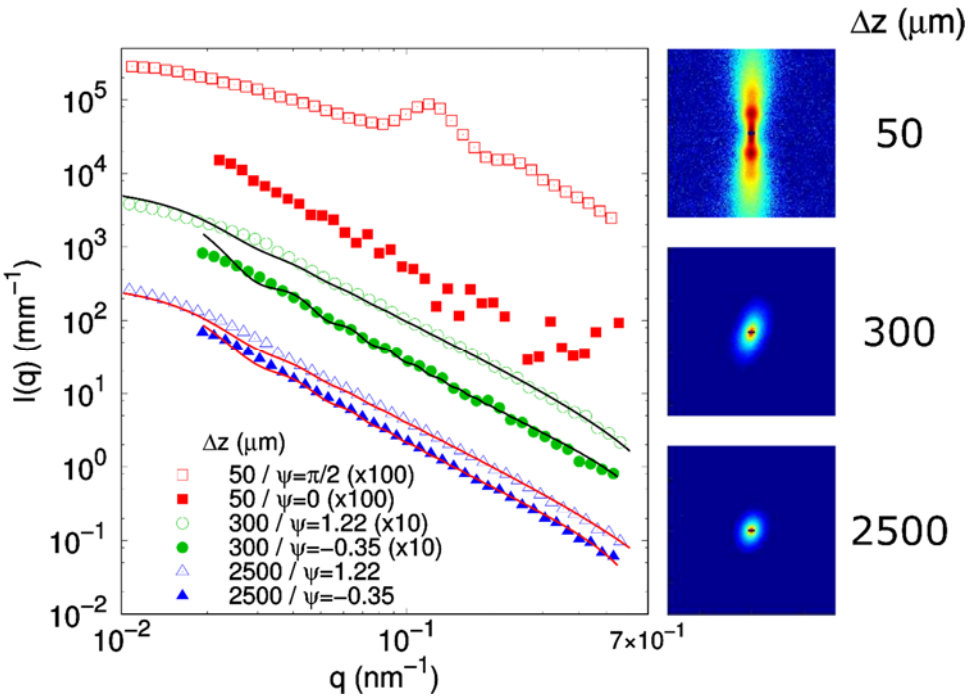

Figure 6: Example of scattering intensities, *I(q)*, and respective two-dimensional patterns of beidellite sample at Δt = 18 min and Δz = 50 (squares), 300 (circles) and 2500 μm (triangles). *I(q)* curves were obtained by integrating the scattering patterns along ψ_0 and $\psi_0 - \pi/2$ over a sector of ±0.044 rad (±2.5°). Data at Δz = 50 μm display a peak due to the presence of $S(q)$. Solid lines refer to the fitting performed with Eq. 6, with m = 1.49 (circles) and 0.70 (triangles).

In Equations 4, 5 and 6, R and a are average radius and thickness of platelets (286 and 0.85 nm, respectively[22,23]). θ and φ are polar and azimuthal angles, where θ is null when the normal to the platelet surface is parallel to z. J_1 is the Bessel function of order 1. $\Delta\rho$ is the difference between scattering length density of beidellite and water and V is the average platelet volume.

Finally, m and N are the width parameter and normalization factor of the ODF, respectively. Selected fit curves are shown in Figure 6. Note that Equation 6 is valid only when the ODF maximum is centered at $\pi/2$. Nevertheless, curve pairs at (ψ_0, $\psi_0-\pi/2$) were treated as ($\pi/2$,0) in order to be fitted.

The platelet concentration profile at different time steps during filtration is reported in Figure 7A, as a function of the distance from the membrane. A very fast increase in volume fraction was detected already after 3 min of filtration. At each time step, $\phi(\Delta z)$ behavior exhibits two distinct regimes. Far from the membrane, ϕ is slowly increasing as Δz decreases. Then, when the concentrations reach the gel transition value, there is a sharp jump in ϕ. In this region, presumably describing the thick deposit, the concentration smoothly increases as much as Δz approaches 0. The concentration profile within this concentrated layer has been described by a heuristic stretched exponential decay:

$$\phi(\Delta z, \Delta t) = \phi_0 + \phi(0, \Delta t) e^{-\left[\frac{\Delta z}{\zeta_b(\Delta t)}\right]^{\omega}} \quad (7)$$

where $\zeta_b(\Delta t)$ is the time-dependent characteristic length of the decay (Supporting Information Table S1) and $\phi(0,\Delta t)$ is the time-dependent colloidal volume fraction at $\Delta z = 0$. At each Δt the stretching factor was $\omega = 0.64$. In Figure 7A, the transition between the two regimes has been simulated by a using a smooth step-function, but just as a guide for the eyes. The fits shown in Figure 7A were performed using $\zeta_b(\Delta t)$, $\phi(0,\Delta t)$ and ω as free parameters, in analogy with Equation 1, where ω is a global parameter which remain constant at every Δz.

Anisotropy parameters and maximum scattering direction, ψ_0, calculated via PCA are shown in Figures 7B and 7C. The strong link between concentration and orientation is qualitatively very similar to the one observed for CNC. Also in this case, the edge of the CPL is well-described by the upturn of orientation degree and angle. In contrast, now the edge is clearly visible even in the concentration profile region related to the sol/gel transition.

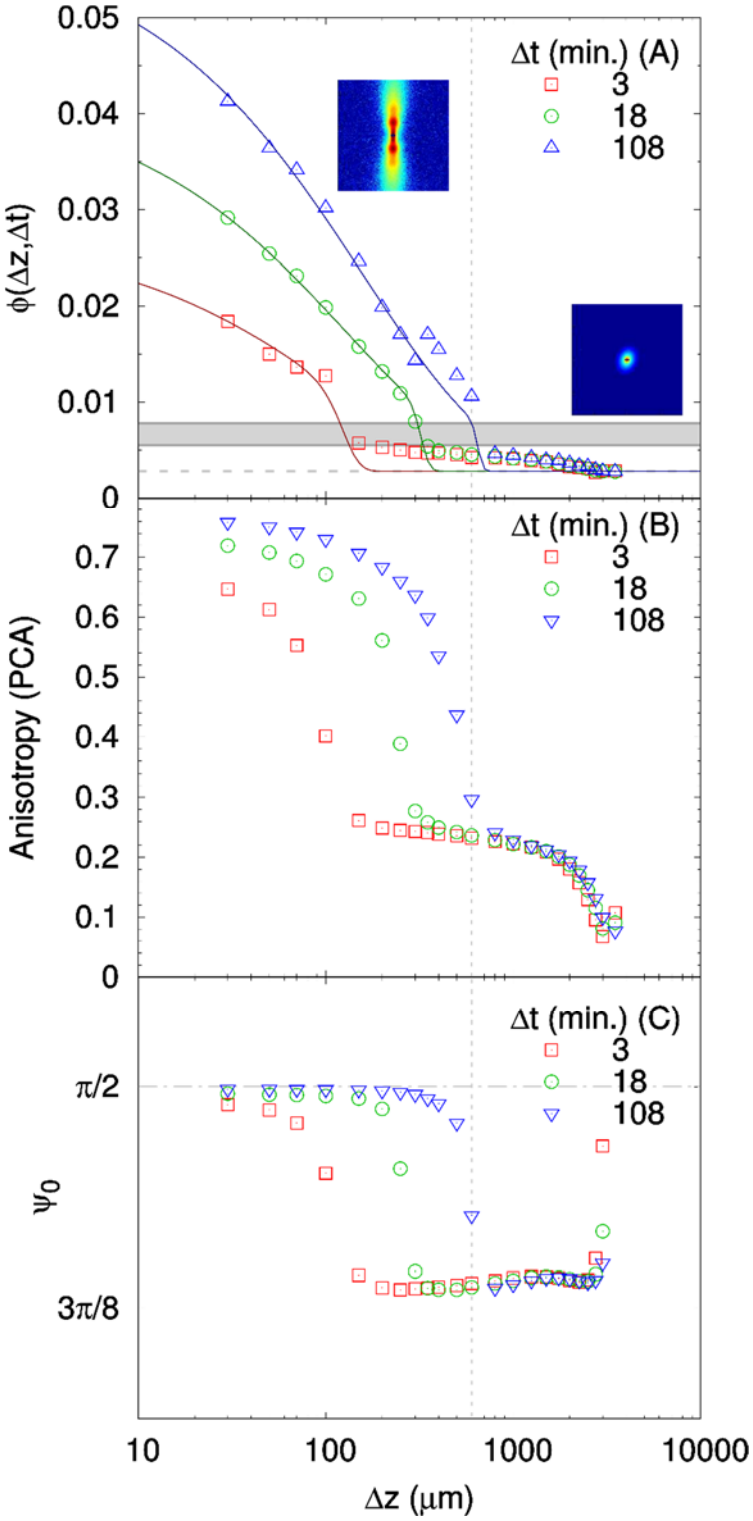

Figure 7: Concentration (A), anisotropy (B) and maximum scattering direction (C) profiles of the growing beidellite deposit as a function of Δz at different time steps. Solid lines in panel (A) refer to the fitting performed with Eq. 7. The two-dimensional scattering patterns in (A) corresponds to Δt = 18 min at Δz = 50 (right) and 2500 μm (left). The vertical dotted line highlights the coupling between concentration and anisotropy and marks the edge of the deposit. The horizontal band marks the concentration of the sol-gel transition.[22]

Anisotropy and orientation angles are defined also in the bulk region close to the deposit. Such values correspond to the average orientation of platelets flowing in the retentate.[25] Compared to CNC, ψ_0 is stabilized at $\pi/2$ rad since the first stages of filtration. This is most likely due to the much higher aspect ratio of the beidellite platelets when compared to the cellulose rods.

Plotting the concentration profiles, $\phi(\Delta z, \Delta t)$, as a function of time (Fig. 8) results once again in an exponential increase:

$$\phi(\Delta z, \Delta t) = \phi_0 + \phi^{\infty}(\Delta z)\left\{1 - e^{-\left[\frac{(\Delta t - t_0)}{\tau_b(\Delta z)}\right]^{\beta}}\right\} \quad (8)$$

where $\tau_b(\Delta z)$ is the characteristic time of the exponential increase and $\beta = 0.42$ is the exponential stretching factor. These fittings allowed to extract the values $\phi^{\infty}(\Delta z)$, $\tau_b(\Delta z)$ and $t_0(\Delta z)$ values for the beidellite CPL. β is a global parameter which remain constant at every Δt.

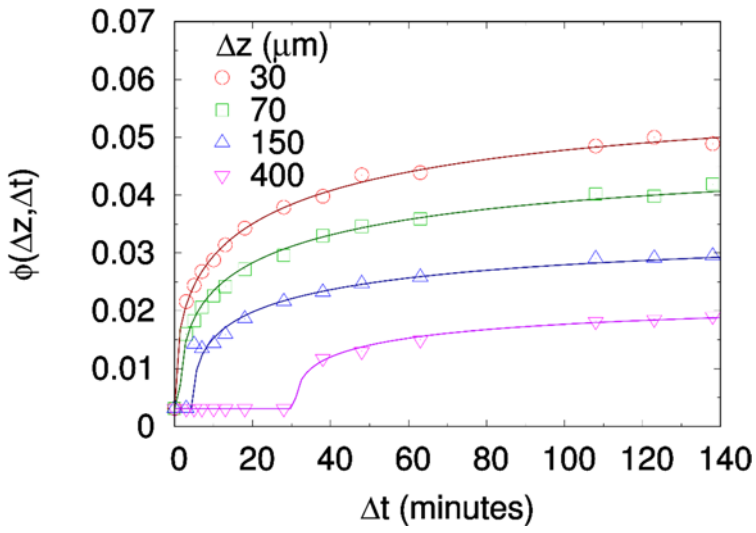

Figure 8: Concentration profiles of the growing beidellite deposit as a function of Δt at different distances from the membrane. Solid lines refer to the fitting performed with Eq. 8.

Even if the PCA method for the determination of the anisotropy is a very powerful tool, it remains qualitative in terms of comparison among different systems. In fact, PCA results

depend on the chosen q-range, particle size and aspect ratio. Therefore, it was very interesting to observe how the partial curves of the ODF width, m, decrease as a function of Δz: specifically, *Anisotropy* $\propto ln(m + 1)$ (Fig. 9A). The reason of this simple relationship was not investigated in the frame of this work. Nevertheless, it gives the opportunity of "mapping" anisotropy values to a quantitative ODF description, even when the scattering model of Equation 6 cannot be applied, as shown in Figure 9B.

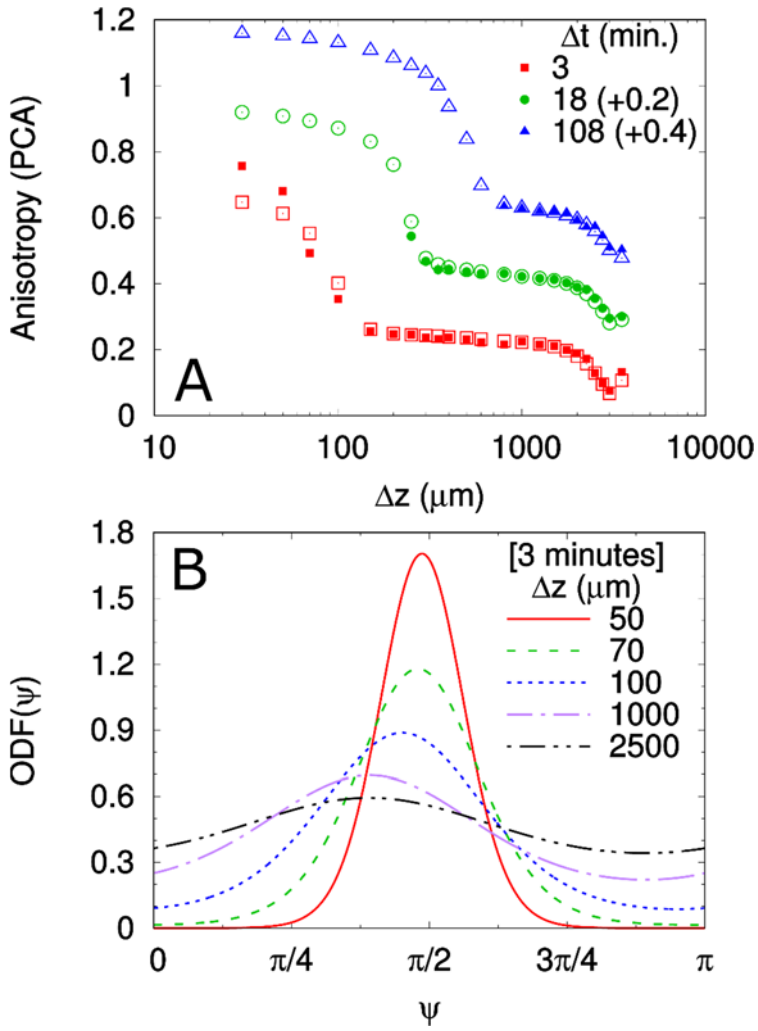

Figure 9: Beidellite system: (A) Comparison between anisotropy values calculated via PCA (empty symbols) and the function α ln(m + 1) from the Maier-Saupe ODF ($\alpha \simeq 0.294$) (full symbols); (B) Plots of Anisotropy Maier-Saupe ODF as a function of ψ at Δt = 3 min and at different distances from the membrane.

Comparison between CNC and Beidellite Systems

In the previous sections, the concentration profiles of CNC and beidellite CPLs have been reported and described by heuristic exponential functions in both space and time scale. Such fittings allowed the extrapolation of curves of interest for cross-filtration processes, i.e. the time-dependence of the colloidal concentration at the membrane, $\phi(0,\Delta t)$ (Fig. 10A), and the concentration profile in the steady state, $\phi^{\infty}(\Delta z)$ (Fig. 10B).

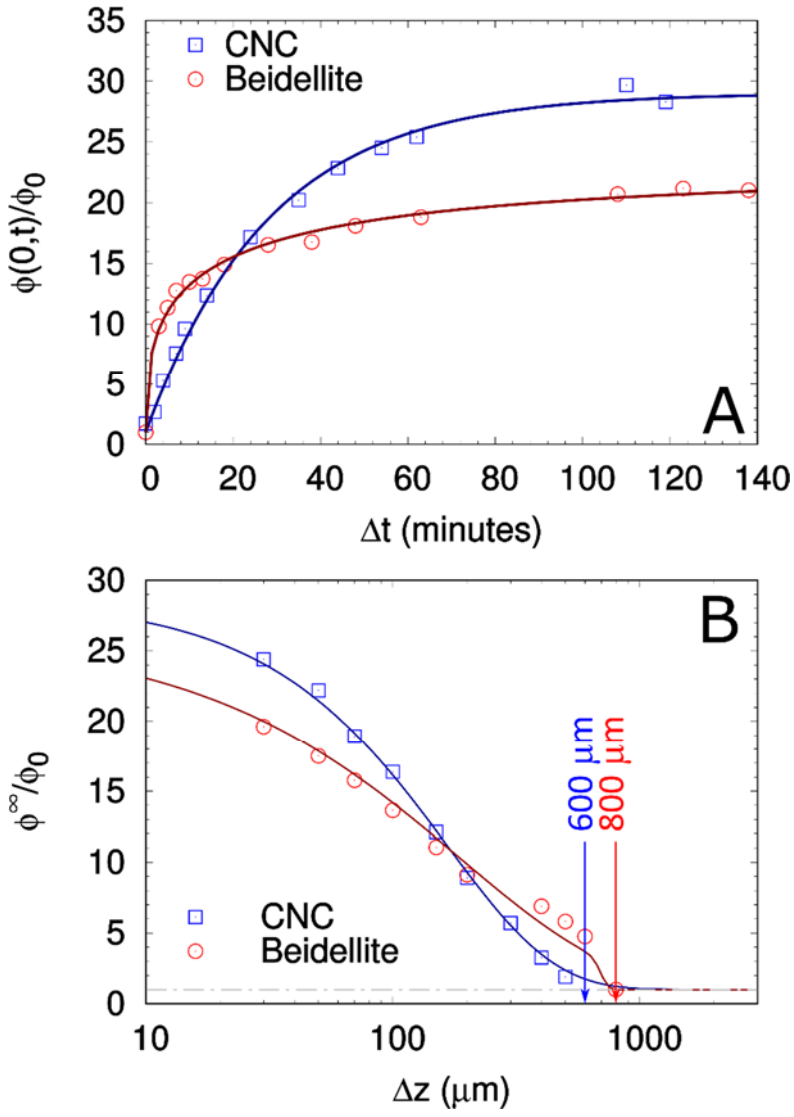

Figure 10: (A) Normalized concentration profiles, extrapolated at $\Delta z = 0$, as a function of Δt. Data for CNC and beidellite systems were obtained by fitting with Eqs. 1 and 7, respectively. Solid lines correspond to fits in agreement with Eqs. 3 and 8. (B) Normalized concentration profiles, extrapolated at $\Delta t \rightarrow \infty$ (steady state), as a function of Δz. Data for CNC and beidellite systems were obtained by fitting

413 with Equations 3 and 8, respectively. Solid lines correspond to fits in agreement with Equations 1 and
414 7.
415
416 In Figure 10A, $\phi(0,\Delta t)$ data are normalized by the initial concentrations. Curves were fitted
417 using the same exponential functions in Equations 3 and 8 for CNC and beidellite systems,
418 consistently with all the profile configurations at any Δz. From this plot, one can observe that
419 beidellite concentration reaches half the asymptotic concentration within the first 6 minutes.
420 Then, during the following about 2 h of observation, it slowly converges to the asymptotic limit,
421 up to about 20 times the initial concentration. The CNC system instead shows a more
422 continuous increase, which is slower at the beginning but then rapidly converge to
423 concentrations about 30 times higher than the initial one.
424 The concentration profile in the steady state, $\phi^{\infty}(\Delta z)$, is displayed in Figure 10B. Equations
425 1 and 7 were used to fit such curves, once again in agreement with all the profile configurations
426 at any Δt. Beidellite concentration profile is flatter compared to the CNC one, simultaneously
427 exhibiting a thicker deposit but with lower relative concentrations close to the membrane. The
428 apparent discrepancies between the values $\phi^{\infty}(0)$ (steady state at the membrane position) are
429 just an artifact of the representation. In fact, in Figure 10A, the asymptotic value is not fully
430 reached, especially in the beidellite plot, whereas in Figure 10B, there is a significant difference
431 between 0 and 10 μm. The extrapolated $\phi^{\infty}(0)$ values are 0.10 and 0.06 for CNC and beidellite
432 systems, respectively.
433 Another interesting set of values is the lag time t_0 as a function of Δz. It provides the time series
434 of the positions at which the measured colloidal volume fraction starts increasing as compared
435 to the bulk concentration ϕ_0 (Figs. 5 and 8), i.e. the position of the upper boundary of the CPL.
436 Therefore, the time-dependent effective thickness of the deposit, $\delta(t)$, can be defined as the
437 inverse of function $\delta(t) \equiv [t_0(\Delta z)]^{-1}$. In Figure 11A, $\delta(t)$ values are reported alongside a tentative
438 extrapolation in the long time range. This was performed by applying Eqs. 3 and 8 for CNC

and beidellite deposits, respectively. In the case of CNC deposit, despite the absence of points after the first 30 minutes, the asymptotic limit of $\delta \simeq 600$ μm matches with the steady state concentration profile, $\phi^{\infty}(\Delta z)$ (Fig. 10B).

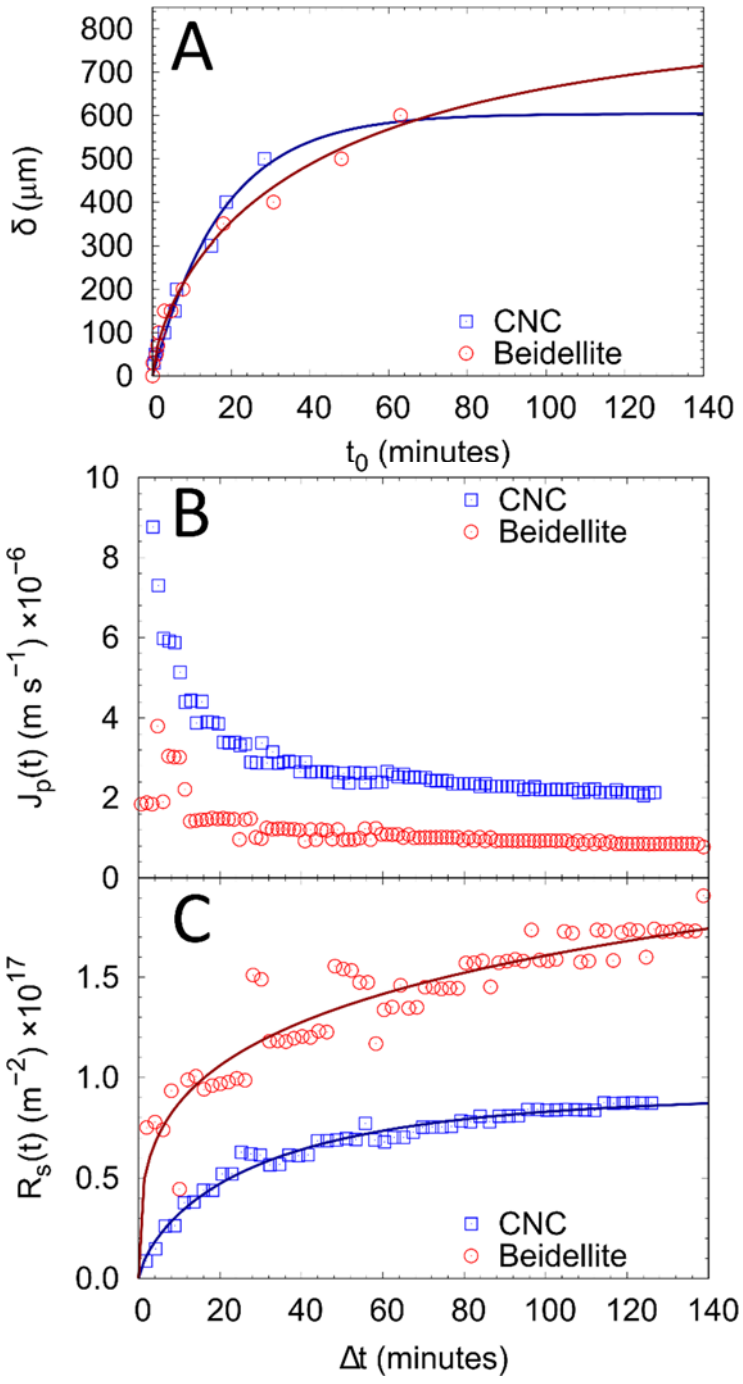

Figure 11: (A) Effective deposit thickness $\delta(t)$ as a function of time $t_0 \equiv \Delta t$. Solid lines for CNC and beidellite systems were obtained by fitting the curves with Equations 3 and 8, respectively. (B) Permeate flux for CNC and beidellite systems. (C) Specific resistance values as a function of time. Solid lines are just a guide for the eyes.

447 One can observe that in this case the limit thickness is achieved after about 30 min. Further
448 CNC cross-filtration does not significantly increase the size of the deposit layer, but strengthens
449 it in terms of both concentration and orientation degree (Fig. 3). On the other hand, the thickness
450 of the beidellite CPL exhibits a slower but persistent increase as a function of time. The fitted
451 curve matches the experimental data within the first 60 minutes (which is about the maximum
452 measured lag time t_0, Figs. 5 and 8), so it is reasonable to extrapolate it toward the asymptotic
453 value of about $\delta \simeq 800$ μm (Fig. 9B). Hence, in contrast to CNC deposit, the beidellite layer
454 needed additional time ($\Delta t > 140$ min) to reach steady state. Such a conclusion was not evident
455 during cross-flow filtration. Indeed, the observation of 2D scattering patterns and permeate
456 fluxes, $J_p(t)$, from both CNC and beidellite experiments showed very weak differences after
457 about 2 h of filtration, qualitatively indicating that the steady state was reached.
458 Another interesting point is that the permeate flux $J_p(t)$ of the CNC suspension is higher than
459 that of the beidellite suspension all along the filtration time (Fig. 11B), while the asymptotic
460 value of the thickness of the CNC deposit ($\delta \simeq 600$ μm) is lower than the one of beidellite ($\delta \simeq$
461 800 μm) (Fig. 10B). Furthermore, the equilibrium volume fraction at the membrane surface of
462 CNC suspension [$\phi^{\infty}(0) = 0.10$] is higher than the one of beidellite suspensions [$\phi^{\infty}(0) = 0.06$].
463 This means that a thinner deposit, even with a higher equilibrium volume fraction at the
464 membrane surface, can induce a higher permeate flux. This observation highlights the
465 complexity of the relationships between the permeation flux and the deposits properties
466 (thickness, equilibrium volume fraction, concentration profile). Hence, the permeability
467 property of the deposits is highly dependent of both the nature of filtered particles (their size,
468 shape, aspect ratio, colloidal interaction), and their structural organization inside the deposits
469 (orientation level, inter particle distance, porosity).

Some of these properties can be enclosed in a single time-dependent function such as the specific resistance of the CPL, $R_s(t)$. It is the resistance parameters per thickness units and is defined by the expression:[29]

$$J_p(t) = \frac{\Delta P}{\mu[R_m + \delta(t)R_s(t)]} \quad (9)$$

where ΔP is the applied transmembrane pressure, μ is the solvent viscosity and R_m is the membrane resistance (respectively $R_m = 5.20 \cdot 10^{12}$ m^{-1} and $R_m = 4.94 \cdot 10^{12}$ m^{-1} during CNC and beidellite experiments). As $\delta(t)$ can be extrapolated in the full time-range, the time-evolution of the specific resistance can be simply calculated from the measured permeate flux (Fig. 11C). These results describe the behavior of $R_s(t)$ in the first minutes after the application of pressure. However, this simplified model does not consider the effect of osmotic pressure within the deposit, which would decrease the effective pressure[8] in Eq. 9. Nevertheless, a lower effective pressure would result in a scaling factor, with negligible effects on the slopes of $R_s(t)$. Another limitation is that $\delta(t)$ has been calculated at one x-position in the cell, while the measured permeate flux is the averaged over their full extension of the membrane. However, all the other pertinent physical quantities, such as concentration, orientation and colloidal shape, are incorporated in the time-dependent specific resistances $R_s(t)$.

In conclusion, the effective functions of $J_p(t)$ not only depend on CPL thickness and particle volume fraction, but parameters like the colloidal aspect-ratio and microstructure (anisotropy degree and orientation angle with respect to the membrane surface of anisotropic colloids) have to be considered. The calculated specific resistance well describes how the physics of these systems is reflected in the filtration parameters. In particular, it is interesting to compare Figures 10A and 11C, as the specific resistance of the beidellite CPL is systematically higher than the CNC system, whereas CNC cake exhibits a higher equilibrium volume fraction. Given that both colloids are stabilized by repulsive electrostatic forces, it can be suggested that the shape and

orientation degree of these particles have a pivotal role in the trend and magnitude of the specific resistance, i.e. on the permeate flux. In CNC fouling layers, despite the equilibrium volume fraction of $\phi^{\infty}(0) = 0.10$, the equilibrium degree of orientation (anisotropy of about 0.5) of these rod-like colloids allows water to pass through the CPL more easily than in beidellite system. In this latter case instead, the clay platelets showed a lower volume fraction along with a higher anisotropy degree, both resulting in a stronger specific resistance to water. From these results, it can be proposed that, in these cases, the differences between the filtration parameters (e.g. CPL thickness, permeate flux, specific resistance) are mainly ascribed to the shape and aspect ratio of the charged-stabilized colloids, which in turn govern the two main features of the microstructure: volume fraction and degree of orientation. Finally, differences in specific resistance seems more linked to the orientation degree rather than to concentration, even though these two parameters are in both cases strongly correlated. This also seems to be confirmed by the fact that the beidellite system shows a strong degree of orientation in the first minutes as compared to the CNC system, where the CPL does not show the same level of anisotropy even at the final stage.

Structural Organization of Dry Deposits at higher Length scales

With the aim of understanding in more details the structural organization on a larger range of lengthscales (form nano- to micrometer), additional ultrafiltration measurements have been performed. One protocol has been developed in order to apply in a first step the same conditions of cross-flow ultrafiltration as the one achieved during *in situ* SAXS measurements, follow by a second step of dead-end filtration. The latter step was used to consolidate the structural organization reached during this first step. Figures 12 and 13 show WAXD patterns and SEM images of dry beidellite and CNC deposits, respectively. These *ex situ* techniques offer the possibility to characterize the structural organization along directions parallel or orthogonal to

519 the film plane. While *in situ* SAXS experiments provided structural information in a parallel
520 geometry, that is in the *xz-plane,* orthogonal observations in the *xy*-plane allowed to access to
521 the structural organization along the velocity (*x)* and transmembrane pressure directions (*y*). In
522 the case of beidellite films analyzed in parallel geometry (Figs. 12B-D), the WAXD pattern
523 exhibit aligned narrow ark reflections, which reveals a strong orientation parallel to the flow
524 direction (Fig. 12C) and the corresponding SEM image show a well-defined layered structure
525 (Fig. 12D). In contrast, the orthogonal WAXD pattern contains rings (Fig. 12F) that, along with
526 the SEM image of one beidellite layer (Fig. 12G), correspond to an isotropic in-plane
527 orientation of the clay platelets. These observations confirmed that during the cross-flow
528 ultrafiltration, under the simultaneous effect of shear flow and transmembrane pressure,
529 beidellite platelets aligned in the direction of the flow and parallel to the membrane surface.
530 Particles are stacked along a direction perpendicular to the membrane surface, forming a well-
531 defined layered structure along the transmembrane pressure direction.

532 The case of dry CNC deposits is more complex as the WAXD patterns suggest a lower
533 degree of orientation of the particles (the description of the reflections in terms of a mixture of
534 two cellulose allomorphs, namely cellulose I and II, is provided in Supplementary Information
535 (Fig. S2). Indeed, a careful examination of the SEM images shows that the film is not
536 homogeneous and contains domains with different organizations. Figures 13D and 13H
537 correspond to a domain where the CNC are parallel to the flow direction and seem to form a
538 layered structure parallel to the membrane. In another region of the film (Figs. 13E and 13I),
539 the fracture surface reveals a layered texture with CNC arches that recalls the patterns observed
540 in chiral nematic arrangements of CNCs. Such an arched organization is observed when the
541 fracture plane is oblique with respect to the helicoidal axis of the cholesteric phase.[29,31] The
542 WAXS patterns in Figure 13C and 13G are thus likely the superimposition of patterns from
543 highly oriented domains (yielding aligned narrow diffraction arks) and less oriented or chiral

544 nematic regions (yielding diffraction rings). In static conditions, CNCs undergo a phase
545 separation into a lower anisotropic phase and an upper isotropic phase providing that the volume
546 fraction exceeds the initial critical concentration ϕ_i of about 0.05. Above a second critical
547 volume fraction ϕ_a of about 0.09, a fully anisotropic chiral nematic phase is obtained, due to
548 the intrinsic chiral character of the rods. The presence of cholesteric domains in the dry deposits
549 is consistent with the high concentration reached upon drying that most probably becomes
550 higher than the second critical concentration. However, the presence of helicoids implies that
551 the nematic organization induced during cross-flow filtration was at least locally suppressed
552 during the dry deposit formation in the second consolidation step or upon pressure release,
553 leading to a relaxation of the organization from nematic to chiral nematic.
554

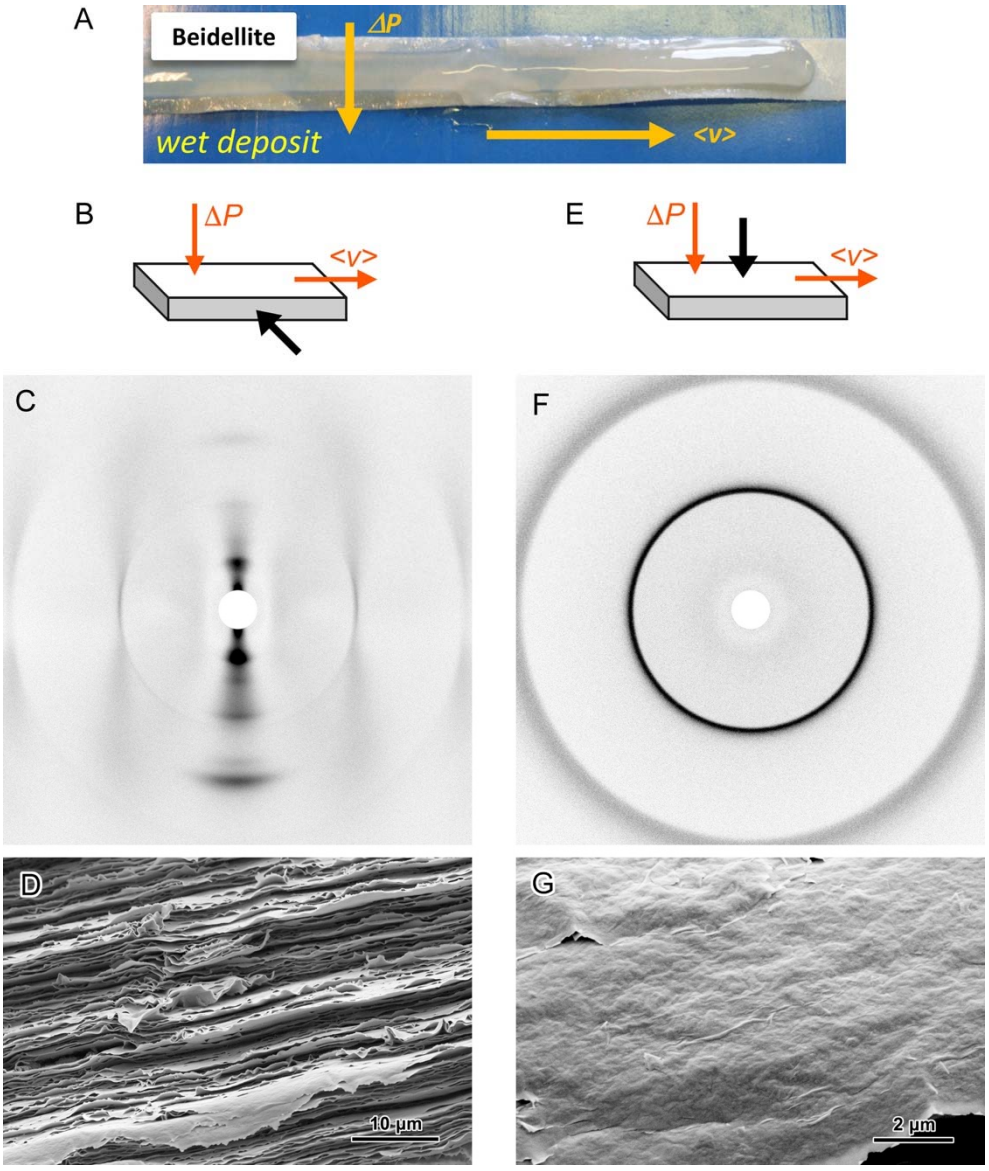

Figure 12: A) Photograph of the beidellite wet deposit (ϕ_0 = 0.0031, 10^{-4} M) obtained by 2 h of cross-flow ultrafiltration (Q = 0.06 L min^{-1}, ΔP = 1.1 × 10^5 Pa) followed by 18 h of dead-end ultrafiltration. Texture analyses of the dry deposit parallel (B-D) and perpendicular (E-G) to the plane of the film. B and E schematically describe the direction of observation (black arrows). C and F are the WAXD patterns of the film. D and G are SEM images of the deposit after a longitudinal fracture (D) of one beidellite layer seen in planar view (G).

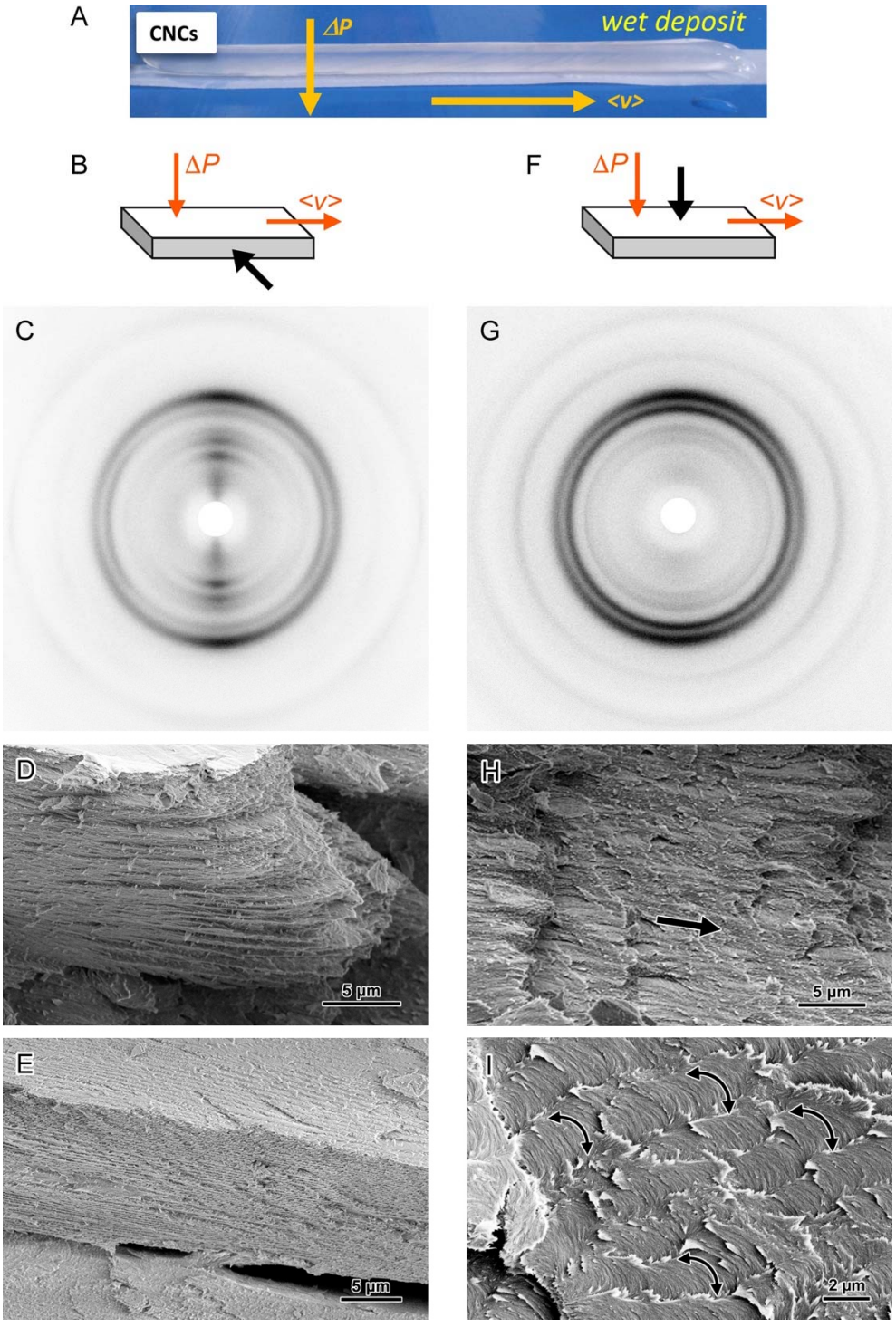

564

565 **Figure 13:** A) Photograph of the CNC wet deposit ($\phi_0 \simeq 0.0044$) obtained by 2 h of cross-flow
566 ultrafiltration ($Q = 0.06$ L min^{-1} $\Delta P = 1.1 \times 10^5$ Pa) followed by 22 h of dead-end ultrafiltration. Texture
567 analyses of the dry deposit parallel (B-E) and perpendicular (F-I) to the plane of the film. B and E
568 schematically describe the direction of observation (black arrows). C and G are the WAXD patterns of
569 the film. D, E, F and I are SEM images of the deposit after a longitudinal fracture (D,E) or in planar
570 view (H,I). The arrows indicate the orientation of the CNCs.

Conclusion

A SAXS study of the concentration polarization layer of either rod- or disk-like charge-stabilized colloids was reported, presenting results in time- and space-scales which were not previously accessible. The spatial resolution and minimal distance from the ultrafiltration membrane of 30 μm, allowed to observe colloidal deposition within the first 2-4 min of the filtration process. The rod-like cellulose nanocrystals system showed a remarkably regular and continuous exponential increase of the colloidal concentration, as a function of both membrane-distance and time. Beidellite clay disk-like particles exhibited a similar behavior, although heuristic stretched-exponential functions had to be used in order to fit the data. Furthermore, the formation of the beidellite concentration polarization layer is clearly affected by the sol-gel transition. Despite these differences, both systems displayed a clear connection between concentration and degree of orientation within the deposit. Both simple and stretched exponential descriptions of concentration profiles were used to extrapolate other characteristics, such as the concentration at the membrane ($\Delta z = 0$) as a function of time, the concentration profile as a function of membrane distance in the steady state ($\Delta t \rightarrow \infty$) and the effective thickness of the concentration polarization layer as a function of time. The latter was successfully used to propose a very simple description of the time-dependence of the specific resistances of both CNC and beidellite fouling cakes, which are directly calculated from the rapid decay of the measured permeate fluxes, including the first few minutes of ultrafiltration. The originality of the structural parameters acquired by the *in situ* SAXS measurements during cross-flow ultrafiltration, allowed discussing in details the potential links between filtration parameters (thickness, resistance and permeate flux) and physical features (colloidal volume fraction, orientation, shape and aspect ratio). It opens up new perspectives in characterization methods at the nanometer lengthscale to better understand the concentration polarization layers phenomena. WAXD analyses and SEM observations of dried deposits obtained after cross-flow

596 followed by dead-end ultrafiltration, allowed to demonstrate that under ultrafiltration, the
597 nanosized platelets assembled into a well-defined layered ultrastructure over micrometer
598 distances. The chiral nematic organization of the CNC deposits have also been evidenced on
599 distances of few tens of micrometers. The characterizations presented in this work demonstrate
600 that ultrafiltration methods can be used to efficiently control the concentration polarization layer
601 of anisotropic nanoparticles, both in terms of both colloidal concentration and orientation which
602 could be extended up to a lengthscale of a few tens of micrometers.

603 ## List of Symbols

604 *a:* Beidellite platelet thickness (m)

605 *c:* Weight percent concentration

606 *D:* Diffusion coefficient (m s^{-2})

607 *d:* Interparticle distance (m^2)

608 *q*: Scattering vector (m^{-1})

609 *F(q):* Scattering form factor (m^{-1})

610 *I(q):* Scattering intensity (m^{-1})

611 *Jp:* Permeate flux (m s^{-1})

612 *m:* Maier-Saupe orientation parameter

613 *N*: Normalization factor

614 *Q*: Cross-flow rate (L min^{-1})

615 *R:* Beidellite platelet radius (m)

616 *Rm:* Membrane resistance (m^{-1})

617 *Rs:* Specific resistance (m^{-2})

618 $S(q)$: Scattering structure factor

619 V: Particle volume (m^3)

620 v: Retentate velocity ($m\ s^{-1}$)

621 β: Stretching parameter (time-dependent concentration profile)

622 ΔP: Transmembrane pressure (Pa)

623 Δz: Distance from the membrane plane (m)

624 $\Delta\rho$: Scattering contrast density (m^{-2})

625 δ: Thickness of the concentration polarization layer (m)

626 ζ: Characteristic length of the exponential decay (concentration profile) (m)

627 θ: Polar angle in spherical coordinates

628 μ: Solvent viscosity (Pa s)

629 τ: Characteristic time of the exponential increase (concentration profile) (s)

630 ϕ: Volume fraction

631 ϕ_0: Initial (retentate) volume fraction

632 ϕ^∞: Equilibrium volume fraction

633 φ: Azimuthal angle in spherical coordinates

634 ψ: Azimuthal scattering angle in the plane (CCD detector)

635 ω: Stretching parameter (length-dependent concentration profile)

636

637

638

Acknowledgement

This work project made in the framework of the NanoCompUV project, has received the financial support of Institut Carnot PolyNat (Investissements d'Avenir - grant agreement #ANR-16-CARN-0025-01). LRP is part of LabEx Tec21 (Investissements d'Avenir - grant agreement no. ANR-11-LABX-0030) and CERMAV is part of LabEx Arcane and CBH-EUR-GS (Investissements d'Avenir - grant agreement #ANR-17-EURE-0003). Both laboratories are part of Glyco@Alps (Investissements d'Avenir - grant agreement #ANR-15-IDEX-02). ESRF is acknowledged for provision of synchrotron beamtime (proposal SC-4612). The authors also thank the Laboratoire Rhéologie et Procédés and ID02-beamline staff for the support, as well as the NanoBio-ICMG Platform (FR 2607, Grenoble) for granting access to the Electron Microscopy facility. Sincere gratitude goes to S. Prévost (Institut Laue-Langevin, Grenoble) for fruitful discussions.

References

(1) Drioli, E.; Giorno, L. (Eds.), Membrane Operations. Innovative Separations and Transformations, Wiley-VCH Verlag GmbH&Co **2009**.

(2) Field, R. W.; Wu, D.; Howell, J. A.; Gupta, B. B. Critical flux concept for microfiltration fouling. *Journal of Membrane Science* **1995**, *100*, 259–272.

(3) Bacchin, P.; Aimar, P.; Sanchez, V. Model for colloidal fouling of membranes. *AIChE Journal* **1995**, *41*, 368–376.

(4) Wijmans, J. G.; Nakao, S.; Van Den Berg, J. W. A.; Troelstra, F. R.; Smolders, C. A. Hydrodynamic resistance of concentration polarization boundary layers in ultrafiltration. *Journal of Membrane Science* **1985**, *22*, 117–135.

(5) Song, L.; Elimelech, M. Theory of concentration polarization in crossflow filtration. *Journal of the Chemical Society, Faraday Transactions* **1995**, *91*, 3389–3398.

(6) Bowen, W. R.; Mongruel, A.; Williams, P. M. Prediction of the rate of cross-flow membrane ultrafiltration: a colloidal interaction approach. *Chemical Engineering Science* **1996**, *51*, 4321–4333.

(7) Jönsson, A.-S.; Jönsson, B. Ultrafiltration of colloidal dispersions: theoretical model of the concentration polarization phenomena. *Journal of Colloid and Interface Science* **1996**, *180*, 504–518.

(8) Elimelech, M.; Bhattacharjee, S. A novel approach for modeling concentration polarization in crossflow membrane filtration based on the equivalence of osmotic pressure model and filtration theory. *Journal of Membrane Science* **1998**, *145*, 223–241.

(9) Bhattacharjee, S.; Kim, A. S.; Elimelech, M. Concentration polarization of interacting solute particles in cross-flow membrane filtration. *Journal of Colloid and Interface Science* **1999**, *212*, 81–99.

(10) Bessiere, Y.; Abidine, N.; Bacchin, P. Low fouling conditions in dead-end filtration: evidence for a critical filtered volume and interpretation using critical osmotic pressure. *Journal of Membrane Science* **2005**, *264*, 37–47.

(11) Bacchin, P.; Si-Hassen, D.; Starov, V.; Clifton, M. J.; Aimar, P. A unifying model for concentration polarization, gel-layer formation and particle deposition in cross-flow membrane filtration of colloidal suspensions. *Chemical Engineering Science* **2002**, *57*, 77–91.

(12) Agashichev, S. P. Enhancement of concentration polarization due to gel accumulated at membrane surface. *Journal of Membrane Science* **2006**, *285*, 96–101.

683 (13) Pignon, F.; Abyan, M.; David, C.; Magnin, A.; Sztucki, M. In situ characterization by
684 SAXS of concentration polarization layers during cross-flow ultrafiltration of laponite
685 dispersions. *Langmuir* **2012**, *28*, 1083–1094.

686 (14) Jin, Y.; Hengl, N.; Baup, S.; Pignon, F.; Gondrexon, N.; Sztucki, M.; Gésan- Guiziou, G.;
687 Magnin, A.; Abyan, M.; Karrouch, M.; Blésès, D. Effects of ultrasound on cross-flow
688 ultrafiltration of skim milk: Characterization from macro-scale to nano-scale. *Journal of*
689 *Membrane Science* **2014**, *470*, 205–218.

690 (15) Jin, Y.; Hengl, N.; Baup, S.; Pignon, F.; Gondrexon, N.; Sztucki, M.; Romdhane, A.;
691 Guillet, A.; Aurousseau, M. Ultrasonic assisted cross-flow ultrafiltration of starch and cellulose
692 nanocrystals suspensions: Characterization at multi-scales. *Carbohydrate Polymers* **2015**, *124*,
693 66–76.

694 (16) Jin, Y.; Hengl, N.; Baup, S.; Maitrejean, G.; Pignon, F. Modeling and analysis of con-
695 centration profiles obtained by in-situ SAXS during cross-flow ultrafiltration of colloids.
696 *Journal of Membrane Science* **2017**, *528*, 34–45.

697 (17) Habibi, Y.; Lucia, L. A.; Rojas, O. J. Cellulose Nanocrystals: Chemistry, self-assembly, and
698 applications. *Chemical Review* **2010**, *110(6)*, 3479–3500.

699 (18) Mitov, M. Chlolesteric liquid crystals in living matter. *Soft Matter* **2017**, *13*, 4176–4209.

700 (19) Kalia, S.; Dufresne, A.; Cherian, B. M.; Kaith, B. S.; Avérous, L.; Niuguna, J.;
701 Nassiopoulo, E. Cellulose-based bio- and nanocomposites: A review. *International Journal of*
702 *Polymer Science* **2011**, *2011*, 837875.

703 (20) Dufresne, A. Nanocellulose: From Nature to High Performance Tailored Materials, 2nd ed.;
704 Walter de Gruyter GmbH: Berlin/Boston, 2017.

(21) Kargarzadeh, H.; Huang, J.; Lin, N.; Ahmad, I.; Mariano, M.; Dufresne, A.; Thomas, S.; Gałęski, A. Recent developments in nanocellulose-based biodegradable polymers, thermoplastic polymers, and porous nanocomposites. *Progress in Polymer Science* **2018**, *87*, 197−227.

(22) Paineau, E.; Antonova, K.; Baravian, C.; Bihannic, I.; Davidson, P.; Dozov, I.; Impéror-Clerc, M.; Levitz, P.; Madsen, A.; Meneau, F.; Michot, L. J. Liquid-crystalline nematic phase in aqueous suspensions of a disk-shaped natural beidellite clay. *Journal of Physical Chemistry B* **2009**, *113*, 15858–15869.

(23) Paineau, E.; Bihannic, I.; Baravian, C.; Philippe, A. M.; Davidson, P.; Levitz, P.; Funari, S. S.; Rochas, C. and Michot, L. J. Aqueous suspensions of natural swelling clay minerals. 1. structure and electrostatic interactions. *Langmuir* **2011**, *27*, 5562–5573.

(24) Gicquel, E.; Bras, J.; Rey, C.; Putaux J.-L.; Pignon F.; Jean B.; Martin C. Impact of sonication on the rheological and colloidal properties of highly concentrated cellulose nanocrystal suspensions. *Cellulose* **2019**, *26*, 7619–7634.

(25) Paineau, E.; Michot, L. J.; Bihannic, I.; Baravian, C. Aqueous suspensions of natural swelling clay minerals. 2. Rheological characterization. *Langmuir* **2011** *27*, 7806-7819.

(26) Narayanan, T.; Sztucki, M.; Van Vaerenbergh, P.; Léonardon, J.; Gorini, J.; Claustre, L.; Sever, F.; Morse, J.; Boesecke, P. A multipurpose instrument for time-resolved ultra-small-angle and coherent X-ray scattering. *Journal of Applied Crystallography* **2018**, *51*, 1–14.

(27) Muthig, M.; Prévost, S.; Orglmeister, R.; Gradzielski, M. SASET: A program for series analysis of small-angle scattering data. *Journal of Applied Crystallography* **2013**, *46*, 1187–1195.

(28) Schütz, C.; Agthe, M.; Fall, A. B.; Gordeyeva, K.; Guccini, V.; Salajková, M.; Plivelic, T. S.; Lagerwall, J. P. F.; Salazar-Alvarez, G.; Bergström, L. Rod packing in chiral nematic cellulose nanocrystal dispersions studied by small-angle X-ray scattering and laser diffraction. *Langmuir* **2015**, *31*, 6507–6513.

(29) Romero, C.; Robert, H. D. Global model of crossflow microfiltration on hydrodynamic particle diffusion based. *Journal of Membrane Science* **1988**, *39*, 157–185.

(30) Maier, W.; Saupe, A. Eine einfache molekular-statistische Theorie der nematischen kristallinflussigen Zustandes. I. *Zeitschrift für Naturforschung* A **1959**, *15*, 882–889.

(31) Majoinen, J.; Kontturi, E.; Ikkala, O.; Gray D.G. SEM imaging of chiral nematic films cast from cellulose nanocrystal suspensions. *Cellulose* **2012**, *19*, 1599–1605.